CrossMark

ORIGINAL ARTICLE

The hydrogen epoch of reionization array dish III: measuring chromaticity of prototype element with reflectometry

Nipanjana Patra[1] ⬤ · **Aaron R. Parsons[1]** · **David R. DeBoer[1]** ·
Nithyanandan Thyagarajan[2,7] · **Aaron Ewall-Wice[15]** · **Gilbert Hsyu[1]** ·
Tsz Kuk Leung[1] · **Cherie K. Day[1]** · **Eloy de Lera Acedo[5]** · **James E. Aguirre[4]** ·
Paul Alexander[5] · **Zaki S. Ali[1]** · **Adam P. Beardsley[2]** · **Judd D. Bowman[2]** ·
Richard F. Bradley[6] · **Chris L. Carilli[5,7]** · **Carina Cheng[1]** · **Joshua S. Dillon[1]** ·
Gcobisa Fadana[8] · **Nicolas Fagnoni[5]** · **Randall Fritz[8]** · **Steve R. Furlanetto[12]** ·
Brian Glendenning[7] · **Bradley Greig[14]** · **Jasper Grobbelaar[8]** ·
Bryna J. Hazelton[9] · **Daniel C. Jacobs[2]** · **Austin Julius[8]** · **MacCalvin Kariseb[8]** ·
Saul A. Kohn[4] · **Anna Lebedeva[1]** · **Telalo Lekalake[8]** · **Adrian Liu[1]** ·
Anita Loots[8] · **David MacMahon[1]** · **Lourence Malan[8]** · **Cresshim Malgas[8]** ·
Matthys Maree[8] · **Zachary Martinot[4]** · **Nathan Mathison[8]** · **Eunice Matsetela[8]** ·
Andrei Mesinger[14] · **Miguel F. Morales[9]** · **Abraham R. Neben[3]** ·
Samantha Pieterse[8] · **Jonathan C. Pober[11]** · **Nima Razavi-Ghods[5]** ·
Jon Ringuette[10] · **James Robnett[7]** · **Kathryn Rosie[8]** · **Raddwine Sell[8]** ·
Craig Smith[8] · **Angelo Syce[8]** · **Max Tegmark[3]** · **Peter K. G. Williams[13]** ·
Haoxuan Zheng[3]

Abstract Spectral structures due to the instrument response is the current limiting factor for the experiments attempting to detect the redshifted 21 cm signal from the Epoch of Reionization (EoR). Recent advances in the delay spectrum methodology for measuring the redshifted 21 cm EoR power spectrum brought new attention

---

✉ Nipanjana Patra
nipanjana@berkeley.edu

[1] University of California at Berkeley, Berkeley, CA, USA

[2] School of Earth and Space Exploration, Arizona State University, Tempe, AZ, USA

[3] Department of Physics, Massachusetts Institute of Technology, Cambridge, MA, USA

[4] Department of Physics and Astronomy, University of Pennsylvania, Philadelphia, PA, USA

to the impact of an antenna's frequency response on the viability of making this challenging measurement. The delay spectrum methodology provides a somewhat straightforward relationship between the time-domain response of an instrument that can be directly measured and the power spectrum modes accessible to a 21 cm EoR experiment. In this paper, we derive the explicit relationship between antenna reflection coefficient (S_{11}) measurements made by a Vector Network Analyzer (VNA) and the extent of additional foreground contaminations in delay space. In the light of this mathematical framework, we examine the chromaticity of a prototype antenna element that will constitute the Hydrogen Epoch of Reionization Array (HERA) between 100 and 200 MHz. These reflectometry measurements exhibit additional structures relative to electromagnetic simulations, but we find that even without any further design improvement, such an antenna element will support measuring spatial k modes with line-of-sight components of $k_\parallel > 0.2h$ Mpc^{-1}. We also find that when combined with the powerful inverse covariance weighting method used in optimal quadratic estimation of redshifted 21 cm power spectra the HERA prototype elements can successfully measure the power spectrum at spatial modes as low as $k_\parallel > 0.1h$ Mpc^{-1}. This work represents a major step toward understanding the HERA antenna element and highlights a straightforward method for characterizing instrument response for future experiments designed to detect the 21 cm EoR power spectrum.

1 Introduction

Since first proposed in [19, 39], measurements of the redshifted 21 cm emission from the primordial neutral hydrogen in the early Universe have gained extraordinary

[5]   Cavendish Astrophysics, University of Cambridge, Cambridge, UK

[6]   National Radio Astronomy Observatory, Charlottesville, VA, USA

[7]   National Radio Astronomy Observatory, Socorro, NM, USA

[8]   SKA-SA, Cape Town, South Africa

[9]   Department of Physics and eScience Institute, University of Washington, Seattle, WA, USA

[10]   Fred Hutchinson Cancer Institute, Seattle, WA, USA

[11]   Department of Physics, Brown University, Providence, RI, USA

[12]   Department of Physics and Astronomy, University of California, Los Angeles, CA, USA

[13]   Harvard-Smithsonian Center for Astrophysics, Cambridge, MA, USA

[14]   Scuola Normale Superiore, Pisa, Italy

[15]   Department of Physics, Massachusetts Institute of Technology, Cambridge, MA, USA

attention as a powerful probe of both cosmology and astrophysics. The science case for 21 cm cosmology, particularly during the Epoch of Reionization, is well established [13, 24, 38]. However, the technical path toward measuring this signal is extremely challenging. The weakness of the hyperfine line keeps the 21 cm signal below the foreground throughout cosmological history and creates sensitivity and calibration challenges that are yet to be fully solved as well as instrument specific. With the system noise temperatures dominated by sky noise and foregrounds that are four to five orders of magnitude brighter than the signal even in the coldest patches of the sky, sky-averaged 21 cm monopole experiments such as Experiment to Detect the Global EoR Signature (EDGES) [5]; Shaped Antenna measurements of the background RAdio Spectrum (SARAS) [32, 33]; Broadband Instrument for Global HydrOgen ReioNisation Signal (BIGHORNS) [40]; SCIHI [48]; Hydrogen Probe of the Epoch of REIonizatioN (HYPERION) [37]; and experiments attempting to detect the 21 cm power spectrum such as the LOw Frequency ARray (LOFAR) [46], the Murchison Widefield Array (MWA) [44], the Giant Meter-wave Radio Telescope (GMRT) [26], the Donald C. Backer Precision Array to Probe the Epoch of Reionization (PAPER) [28], the Hydrogen Epoch of Reionization Array (HERA) [9], and the future Square Kilometer Array (SKA[1],) [21, 42] must furnish their foreground suppression limits given their system performance at levels significantly beyond anything previously achieved in radio telescopes operating below 1 GHz.

The response of a radio telescope, either a single dish or an interferometer, modulates spectrally smooth foregrounds, contaminating spectral modes that might otherwise be used to measure reionization [4, 7, 17, 23, 45, 47]. Moreover, measurement sensitivity that can be increased by increasing the collecting area of the element using reflector structures, results in increased element size. However, the chromaticity of a reflector dish scales with its diameter, putting the needs of foreground suppression and signal sensitivity in direct tension with one another. A major step forward for the field of 21 cm cosmology has been the development of a mathematical description of telescope chromaticity, how it varies with element separation (or telescope diameter), and what it implies for distinguishing the foreground emission from the cosmological 21 cm signal [10, 16, 17, 29, 41, 42, 45, 47]. The "wedge", as it is colloquially known, describes a linear relationship between the separation between elements in an interferometric baseline and the maximum line-of-sight Fourier mode[2] that may be occupied by smooth spectrum foreground emission. At low-order $k_\parallel$ modes within the limits of the wedge, foreground contamination may be suppressed through a combination of calibration and model subtraction. However, calibration or modeling errors rapidly re-establish the characteristic wedge pattern [2]. Outside of the wedge, foreground contamination drops rapidly [11, 14, 35, 43], provided that the spectral responses of antenna elements and analog

---

[1]www.skatelescope.org

[2]Assuming a flat sky and using appropriate cosmological scalars, the spectral axis, ν, and angle on the sky, $\vec{\theta}$, translate to coordinates in a three-dimensional volume at cosmological distances. In describing the spatial power spectrum of emission $P(\vec{k})$ in this volume, we use the three-dimensional wave vector $\vec{k} \equiv (k_\parallel, \vec{k}_\perp)$, where $k_\parallel$ is the line of sight component aligned with the spectral axis, ν, and $\vec{k}_\perp$ lies in the plane of the sky.

electronics are sufficiently smooth.[3] In the avoidance-based foreground strategy employed by PAPER [1, 31], these modes may be targeted as the lowest risk path for constraining 21 cm reionization in the near term.

The efficacy of foreground removal from the measured data critically limits the 21 cm power spectrum measurements. The delay transformation technique of foreground removal [27, 28, 30], computes the Fourier transform of the visibility measured by an interferometer and produces a spectrum, referred to as the delay spectrum hereafter, which is a function of the geometric time delay corresponding to the physical length of the baseline between two antennas. For the visibilities measured over a wide field across a wide frequency bandwidth, the delay spectrum consists of the convolution of the instrument response with the foreground signal, and the 21cm power spectrum, hereafter referred to as the EoR signal. The technique exploits the smooth spectral characteristics of the foreground and for a visibility measurement by an interferometer with a baseline b, confines the foreground contribution to the computed delay spectrum within the largest possible time delay, $\tau_g = b/c$, corresponding to the given baseline length. In reality, however, foregrounds show a response beyond the maximum geometric delay due to broadband spectrum of the foreground sources and chromatic instrument response. For an ideal system, this is a rapidly diminishing response beyond τ_g spanning the delay range corresponding to the inverse of the measurement bandwidth. Beyond this limit, for an ideal system performance, the delay spectrum would be dominated by any signal with spectral and spatial fluctuations over small scales, such as the EoR signal. The interaction between the sky signal and instrument response can alter the relative contribution of the foreground, and the EoR signal at a given delay and influence the detectability of the EoR signal. These interactions can cause the foreground to spill over into higher delays where EoR power spectrum can be estimated.

In this paper, we use reflectometry measurements to investigate the delay-domain performance of a HERA element design that is currently operational at the Karoo desert in South Africa in the midband observation frequency 100–200 MHz. The element design consists of 14 m paraboloidal reflector dish and a crossed dipole feed (Fig. 1) operating from 100 to 200 MHz. For clarity, the return loss of the feed when measured off of the dish will be referred to as "feed return loss" hereafter. The dish-feed assembly, when the feed is placed at the focal point of the dish is referred to as "HERA element" hereafter.

This paper is one in a series of five papers to study the time and frequency domain performance of the HERA element for the midband operation (100–200 MHz). We compare reflectometry measurements to the specifications set by the time and frequency domain simulation of the HERA element [9, 12, 25] and to the specification of EoR to foreground power ratio established by [42]. The paper is organized as follows. Section 2 briefly describes the delay spectrum for the ideal and real performance of a two element interferometer. Section 3 describes the reflectometry measurements and establishes the connection between visibility measurements and

---

[3]Here, we distinguish the chromaticity of the elements in isolation from the chromaticity inherent to element separation in an interferometric baseline.

Fig. 1 Top: The HERA feed consists of a pair of crossed-dipoles over 1.72 m diameter backplane made of wire mesh. The backplane is surrounded by 0.36 m wide wire mesh around the edge resulting in encasing the crossed-dipoles in a cylindrical cage. Bottom: A prototype HERA element at the Green Bank NRAO site consisting of a crossed dipole feed and a paraboloidal reflector dish

reflectometry. Reflectometry results are described in Section 4. Section 5 evaluates the performance of the HERA element for detection of the 21 cm power spectrum.

2 Visibility measurements by a two element interferometer: the delay spectrum

For a two element interferometer with a baseline $\vec{b}$ and antenna voltage gain patterns a_1, a_2, the voltage at the output of each antenna element is,

$$v_1(\hat{\theta}, \nu) = a_1(\hat{\theta}, \nu)\, v_{\text{sky}}(\hat{\theta}, \nu)$$

$$v_2(\hat{\theta}, \nu) = a_2(\hat{\theta}, \nu)\, v_{\text{sky}}(\hat{\theta}, \nu)\, e^{2\pi i \nu \vec{b}\cdot\hat{\theta}/c}$$

where, $v_{\text{sky}}(\hat{\theta}, \nu)$ is the sky voltage in the direction $\hat{\theta}$ at a frequency ν. The measured visibility is,

$$V(\vec{b}, \nu) = \langle \int A(\hat{\theta}, \nu)\, I_{\text{sky}}(\hat{\theta}, \nu)\, e^{-2\pi i \nu \vec{b}\cdot\hat{\theta}/c} d\Omega \rangle$$

$$= \int A(\hat{\theta}, \nu)\, I_{\text{sky}}(\hat{\theta}, \nu)\, e^{-2\pi i \nu \vec{b}\cdot\hat{\theta}/c} d\Omega \tag{1}$$

where $A(\hat{\theta}, \nu) = a_1(\hat{\theta}, \nu) \, a_2^*(\hat{\theta}, \nu)$ is the cross power pattern and $I_{\text{sky}}(\hat{\theta}, \nu) = v_{\text{sky}}(\hat{\theta}, \nu) \, v_{\text{sky}}^*(\hat{\theta}, \nu)$ is the sky intensity. The Fourier transform of the visibility along the frequency axis i.e, the delay spectrum is [30],

$$
\tilde{V}(\vec{b}, \tau) = A(\vec{b}, \tau) * I_{\text{sky}}(\vec{b}, \tau)
$$
$$
= \int_{-\infty}^{\infty} A(\tau - \Delta\tau) I_{\text{sky}}(\tau) d\Delta\tau \tag{2}
$$

The delay-transformed visibility is related to the power spectrum of redshifted 21 cm emission by the relation,

$$
P_{21}(\vec{k}_\perp, k_\parallel) \approx |\tilde{V}(\vec{b}, \tau)|^2 \left(\frac{\lambda^2}{2k_B}\right)^2 \frac{1}{\Omega \Delta B} \left(\frac{D^2 \Delta D}{\Delta B}\right) \tag{3}
$$

where

$$
\vec{k}_\perp = \frac{2\pi f}{D}\left(\frac{\vec{b}}{c}\right), \quad k_\parallel = \frac{2\pi \tau \, f_{21} H(z)}{c(1+z)^2}, \tag{4}
$$

- $f_{21}, f, z, \Delta B$: rest frame, observation frequency of the 21 cm radiation and redshift and bandwidth of observation.
- k_B: Boltzmann constant.
- $D \equiv D(z)$ transverse comoving distance along the line of sight, ΔD is the comoving depth along the line of site corresponding to the bandwidth ΔB.
- $H(z) = H_0[\Omega_M(1+z)^3 + \Omega_R(1+z)^2 + \Omega_\Lambda]^{1/2}$
  is the Hubble constant as a function of redshift, $H_0 = 100h$ km s^{-1} Mpc^{-1}, $\Omega_M = 0.27$, $\Omega_R = 0.73$, $\Omega_\Lambda = 1 - \Omega_M - \Omega_R$ are the matter, radiation and dark energy density parameters respectively.
- $P_{21}(\vec{k}_\perp, k_\parallel)$ is in units of K^2 $(h^{-1}\text{Mpc})^3$
- $\Omega \Delta B = \int \int |A(\hat{\theta}, \nu)|^2 d\Omega d\nu$ is related to the spatial volume probed by the instrument (see [31]).

3 Effects of multiple reflections on visibility and delay spectrum

HERA consists of paraboloidal reflector antennas which provide increased collecting area per array element compared to its predecessor experiment PAPER. Plane waves incident on a prime focus paraboloidal dish are focussed at the feed which is at the focal plane of the dish. The mismatch between the impedance of free space with the feed and transmission line results in a partial coupling of the sky signal while the rest is reflected off of the feed. This signal illuminates the dish and most of it is reflected back into space. However, a part of it reflects back and forth several times between the feed and the vertex of the dish which is shadowed by the feed. Such reflections generate multiple copies of the incident sky signal of reduced strength at various delays producing additional correlations in the visibilities data. An identical response can result from reflections internal to the system, for example between antenna output and backend receiver input causing similar signal contamination in delay space. We

measure the system response to estimate these reflections and the resulting effects in power spectrum measurements.

To develop the mathematical formalism for multipath propagation between the feed and the dish, we make the following assumptions. We assume that the reflection coefficient of the paraboloidal dish is proportional to its area of illumination i.e, upon complete illumination of the dish by a plane wave, 100% of the incident radiation is reflection off of the dish and reflection coefficient of the dish is unity. The sky voltage incident on the dish illuminates the part of the dish that is not shadowed by the feed. The corresponding dish reflection coefficient is denoted as $(1 - \Gamma_d)$ which is complex. The dish reflection coefficient of the part of the dish shadowed by the feed is denoted by Γ_d. The reflection coefficients also absorbs a few physical details such as divergence/convergence of the downward/upward traveling signal due to geometry of the dish which are not explicitly mentioned in the equations. However, the equations are sufficient for building intuition about the antenna element delay spectrum and it's impact on measurements of the redshifted 21 cm power spectrum. The voltage reflection coefficient of the feed is Γ_f and corresponding transmission coefficient is $(1 + \Gamma_f)$ (see, e.g. Pozar). Both Γ_d and Γ_f are complex numbers that are functions of frequencies.

For a first incidence of the sky voltage v_{sky} (Fig. 2), $(1 - \Gamma_d)(1 + \Gamma_f)$ fraction of it is coupled into the cable leading to the receiver backend from the feed whereas Γ_f fraction of it is reflected and reradiated off of the feed. This subsequently undergoes Γ'_d reflection off of the dish and $(1 + \Gamma_f)$ of it re-enters the feed with a roundtrip time delay $\Delta\tau = 2F/c$ where F is the focal length of the dish. Notable here is, at the frequencies where the dish is at the far field of the feed, the reflected wave will be a plane wave at the time of second reflection off of the dish and $\Gamma'_d = \Gamma_d$. HERA paraboloidal dish focal length is 5 m which, correspond to the far field of the dipole only at frequencies > 120 MHz (Fig. 3). At frequencies where the dish is in the near field of the feed, the wavefront reflected off of the feed will still be spherical when they reach the dish for the second reflection and dish reflection coefficient Γ'_d will be different from Γ_d. Multiple reflections of the spherical wave between the feed and
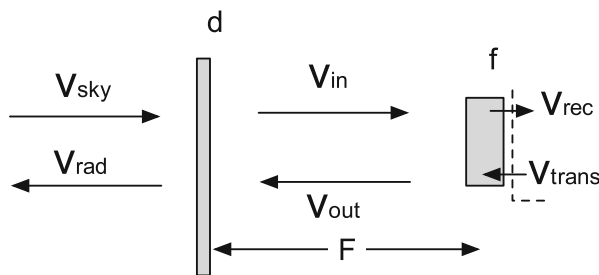

Fig. 2 Schematic diagram of signal propagation through the dish and the feed of during both transmission and reception. V_{sky}, V_{in} and V_{rec} represents the sky voltage, total reflected voltage from the dish that is incident on the feed and the net received voltage at the receiver input. In transmission mode, V_{trans}, V_{out} and V_{rad} are the voltage transmitted by the network analyzer, the voltage output of the feed and the the net radiated voltage after reflection on the dish. Γ_d, Γ_f are the voltage reflection coefficients of the dish and the feed
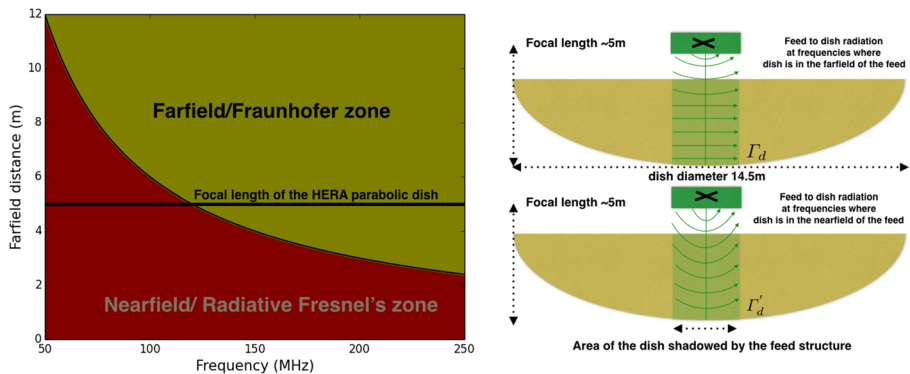
Fig. 3 Left: The farfield distance of the HERA feed dipole as a function of frequencies. At frequencies below 120 MHz the dish is within the Frenel zone. Right: Schematic description of the difference between the feed-dish multiple reflections when the dish is in the Fresnels zone and in Fraunhofer zone

the dish apex will result in leakage of polarized radiation to the orthogonal dipole. This results in is a direction independent polarization leakage effect of which effect of which in power spectrum measurements will be considered in a forthcoming paper. But for the sake of generality and distinguishing the spherical and plane wave case, we write the reflection coefficient of the dish for the second and the higher order reflections as Γ'_d. Hence, if v_{sky} is reflected n times in between the feed and the dish, the net voltage entering the feed after the nth reflection can be written as:

$$v_{rec} = (1 - \Gamma_d)(1 + \Gamma_f)v_{sky}[1 + \Gamma_f\Gamma'_d e^{2\pi i v\Delta\tau}$$
$$+ (\Gamma_f\Gamma'_d)^2(e^{2\pi i v\Delta\tau})^2 +$$
$$.... + (\Gamma_f\Gamma'_d)^n(e^{2\pi i v\Delta\tau})^n] \tag{5}$$

or,

$$\frac{v_{rec}}{v_{sky}} = (1 - \Gamma_d)(1 + \Gamma_f)\sum_{n=0}^{N}[\Gamma_f\Gamma'_d e^{2\pi i v\Delta\tau}]^n \tag{6}$$

Note that $n = 0$ is when the initial wave enters the cable at the feed (where we assume we have set our reference plane).

An accurate measurement of this quantity requires receiving v_{sky} from a well calibrated, wideband source in the sky in the far field of the HERA antenna element with significant isotropic emission. While this condition is hard to achieve in practice, reciprocity of the antenna performance in the transmission and reception mode implies the right hand side of (6) could be measured using the return loss measurement technique with a vector network analyzer (VNA). VNA measurements are done by connecting a passive balun to the feed. This exercise provides a conservative estimate and a baseline for further improving the antenna impedance mismatch by using a matching network. During observations, the passive balun will be replaced by an active balun that incorporates the matching network. While a matching network can change the absolute amplitude of the reflections, the frequency structures imprinted

due to the reflections in the feed and the dish will still critically affect the instrument response.

4 Reflectometry measurements

Reflectometry measurements determine the multiple reflection of any signal within a system in either time [34] or frequency domain. We carried out frequency domain reflectometry on a prototype HERA element in Green Bank, WV (Fig. 1) in order to measure the response of the feed and dish assembly. The prototype HERA element consists of a 14.5 m diameter paraboloidal reflector and a crossed-dipole pair as a feed. The cross dipole antenna pair is identical to the feed of the PAPER antenna and suspended at the focal plane of the dish with the support of three vertical poles. HERA elements will be closely spaced with center to center distance between the two adjacent dishes slightly larger than the dish diameter. The crossed dipole feed is encased in a cylindrical cage with the back plane to reduce the coupling between the adjacent dishes. The feed is raised and lowered by a pulley system mounted on the three poles. The focal height of the dish is $\approx$ 5 m. The detail geometry and electromagnetic design of of the feed is presented in [9].

During the oberservation, each HERA element is connected to an active balun similar to the ones used in the PAPER antenna which provides greater than 10dB return loss of power at the feed output. For the instrument delay response measurements presented here, the active balun is replaced by a passive one with 2:1 impedance ratio to match the impedance of the 50 Ω transmission line. These measurements, therefore, provide a conservative estimate for Γ_f and s_{11}. The true element response requires de-embedding the balun response from this measurements. However, the four port measurements of the balun shows a $>$ 23 dB return loss at the balun input and 0.1 dB transmission loss through the balun both of which are smooth across frequency and does not alter the results. For simplicity we ignore de-embedding the balun response. Accurate estimate of the element delay response will require de-embedding the balun response from the measurements and modify the de-embedded response by expected impedance mismatch between the antenna and active balun. This will be considered elsewhere when the active balun and the receiver backend design of the individual HERA element will be completed.

4.1 Measurement equations

The measurement presented here is done using a vector network analyzer (VNA) that is connected to the antenna using a 15 m long LMR 400 cable. This length correspond to a 120 ns roundtrip delay. A VNA is connected to the HERA element via a $\approx$ 15 m cable that transmits a broadband noise voltage, v_{trans}. A $(1 + \Gamma_f)$ factor of this voltage is radiated by the feed while the fraction Γ_f returns to the VNA. The transmitted signal illuminates the dish and most of it is radiated into the free space, a fraction Γ_d of this signal is reflected back toward the feed, and $(1 + \Gamma_f)$ fraction of it is received by the VNA. The received voltage, after n reflections between the dish and the feed (where again $n = 0$ is the first reflected signal at the reference plane), is

therefore:

$$
\begin{aligned}
v_{rec} &= \Gamma_f v_{trans} \\
&+ v_{trans}(1 + \Gamma_f)^2 \Gamma'_d e^{2\pi i v \Delta \tau} \\
&+ v_{trans}(1 + \Gamma_f)^2 \Gamma_d 6\prime e^{2\pi i v \Delta \tau} \Gamma_d \Gamma_f e^{2\pi i v \Delta \tau} \\
&+ v_{trans}(1 + \Gamma_f)^2 \Gamma'_d e^{2\pi i v \Delta \tau} (\Gamma_d \Gamma_f e^{2\pi i v \Delta \tau})^2 \\
&\dots + v_{trans}(1 + \Gamma_f)^2 \Gamma'_d e^{2\pi i v \Delta \tau} (\Gamma_d \Gamma_f e^{2\pi i v \Delta \tau})^n
\end{aligned}
\tag{7}
$$

or,

$$
\frac{v_{rec}}{v_{trans}} = \Gamma_f + \frac{(1 + \Gamma_f)^2}{\Gamma_f} \sum_{n=1}^{N} [\Gamma_f \Gamma'_d e^{2\pi i v \Delta \tau}]^n
\tag{8}
$$

The VNA measures the quantity $v_{rec}/v_{trans} = s_{11}$ which is the voltage reflection coefficient of the HERA element. The fundamental difference between the (6) represents the system response in reception mode while our measurements are done in transmission mode (8). The $n = 0$ term in (6) represents the transmission of the beam integrated sky signal from the antenna to the transmission line while the same in (8) represents the reflection at the antenna terminal and the transmission line. The zero delay response in the transmission mode is identical whether or not the feed is suspended on the dish. Therefore, we measure the feed return loss alone while the feed is kept on the ground facing the sky. This measurement includes reflections from the surrounding cage structure but exclude the dish response. Using the measurement of the feed reflection coefficients (Γ_f), the refection coefficient s_{11} of the dish and feed assembly is corrected via (10). Writing $v_{rec}/v_{trans} = s_{11}$, (8) can be written as,

$$
s_{11} + \frac{(1 + \Gamma_f)^2}{\Gamma_f} - \Gamma_f = \frac{(1 + \Gamma_f)^2}{\Gamma_f} \sum_{n=0}^{N} [\Gamma_f \Gamma'_d e^{2\pi i v \Delta \tau}]^n
\tag{9}
$$

Finally,

$$
\frac{v_{rec}}{v_{sky}} = (1 - \Gamma_d) \left[(1 + \Gamma_f) + \frac{\Gamma_f}{(1 + \Gamma_f)} (s_{11} - \Gamma_f) \right]
\tag{10}
$$

From this, for a two element interferometer with identical antenna elements, the ratio of the received sky intensity to true sky intensity will be,

$$
\begin{aligned}
\frac{I_{rec}}{I_{sky}} &= \left| \frac{v_{rec}}{v_{sky}} \right|^2 = |1 - \Gamma_d|^2 \times \\
&\quad [|1 + \Gamma_f|^2 + 2 \operatorname{Re} \left((1 + \Gamma_f)^* \frac{\Gamma_f}{(1 + \Gamma_f)} (s_{11} - \Gamma_f) \right) \\
&\quad + \frac{|\Gamma_f|^2}{|1 + \Gamma_f|^2} |s_{11} - \Gamma_f|^2]
\end{aligned}
\tag{11}
$$

In terms of visibility, the same could be written as,

$$V^{mul}(\vec{b}, \nu) = \int |1 - \Gamma_d|^2 \times$$

$$[|1 + \Gamma_f|^2 + 2\,\mathrm{Re}\left((1 + \Gamma_f)^* \frac{\Gamma_f}{(1 + \Gamma_f)}(s_{11} - \Gamma_f)\right)$$

$$+ \frac{|\Gamma_f|^2}{|1 + \Gamma_f|^2}|s_{11} - \Gamma_f|^2]I_{sky}e^{-2\pi i\nu\vec{b}\cdot\hat{\theta}/c}d\Omega \tag{12}$$

Comparing (12) and (1), the cross power generated by ν_1 and ν_2 has a spurious visibility response due to mutual correlation between multiply reflected voltages represented by the second and the third term of the right hand side of (12). In the ideal case, $\Gamma_f = 0$, in which case (12) results in (1). The Fourier transform of this visibility spectrum along the frequency axis results in the delay spectrum. In the delay domain, visibilities contributed by any two voltage components from two antennas with no mutual delay will be located at the delay $\tau = 0$ whereas any two voltage components from two antennas having a mutual delay of $n\Delta\tau$ will be centered at $n\Delta\tau$. These will result in leakage of the foreground to delays where EoR power spectrum could be measured.

The delay transform of the measured return loss is sensitive to the bandwidth of measurements. Wideband measurements over finite bandwidth are analogous to windowing the frequency domain data by a square window function that results in multiple side lobes at higher delays. We apply the Blackman-Harris window function of [42] to estimate the delay transform.

4.2 Results

Return loss measurements of the feed as well as HERA element iare shown in Fig. 4. Corresponding delay spectra are shown in Fig. 5. The delay spectra of the feed and the HERA element closely follow each other up to delays < 30 ns. Figure 6 shows the delay spectra estimated using a square window as well as Blackman-Harris window. In this case, the delay spectra follow each other up to 30 ns and start deviating after that. This is because at small delays the spectrum is dominated by the small scale reflections associated with the feed cage. Above 50 ns, the windowing effect begins to manifest. The relevant length scales inside the system from where the reflections are expected and the corresponding delays are summarized in the Table 1. The delay spectrum of the feed exclude the dish reflections. However, the VNA reflections at the VNA input are present in both the cases. We measure the VNA input reflections by connecting an open load at the feed input of the cable that results in 100% signal reflection. The combined effect of the VNA input return loss along with the cable resistive loss is shown in figure (Fig. 5). Since our measurement plane is at the open end of the cable, first reflection appears at zero delay while the second one appears around 120 ns. which is ≈ -22 dB. Third and consecutive reflections are buried in the noise floor of this measurement. Therefore, if the return loss at the backend input is > 22 dB, the delay spectrum contamination due to the reflection at the receiver input will be negligible. Moreover, if the cable length is sufficiently increased without
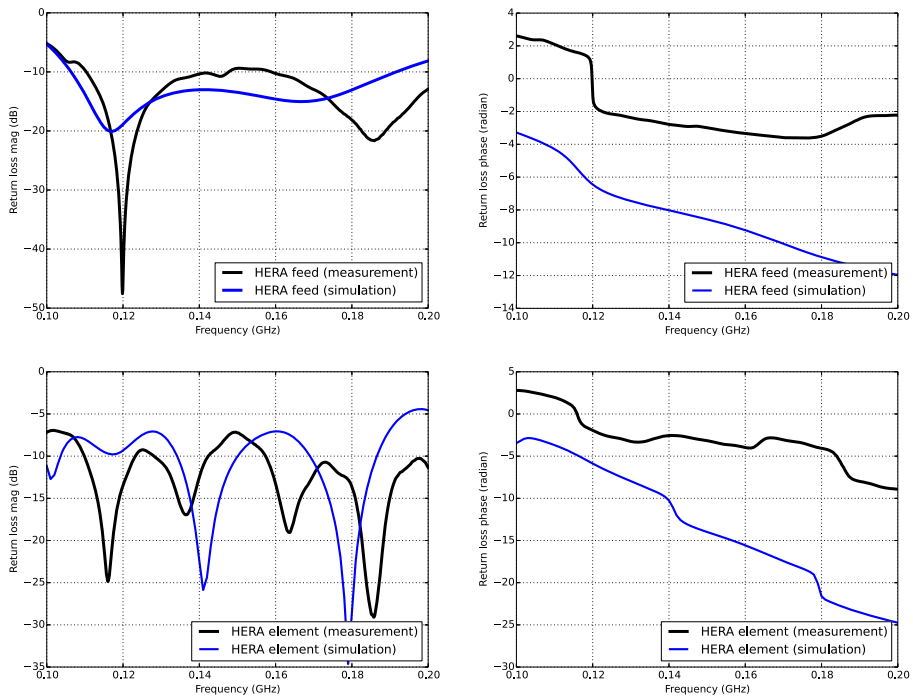
Fig. 4 Upper panel: Magnitude and phase of the return loss of the feed as simulated and measured. Both measurement and simulation shows similar level of return loss across the band with marginally better return loss at the high frequency end of the band. Lower panel: Magnitude and phase of return loss when the feed is suspended at the focal point of the dish which 5 m above the dish vertex

the loss of signal, these reflections could be made to occur at delays which are not of interest for EoR measurements.

4.3 Comparison with simulations

4.3.1 HFSS electromagnetic simulation

Performance of the HERA feed and the HERA element is simulated using the EM solver "High Frequency Structural Simulator (HFSS)" using the finite element method. These simulations provide a ballpark estimate of the system response under various ideal conditions. The measurement is in agreement with the simulation in some aspects and differ in some. The simulated return loss of the feed by HFSS, both magnitude and phase are shown in the upper panel of Fig. 4 along with the measurements. Bottom panel of Fig. 4 shows the same when feed is suspended at the focal plane of the paraboloidal dish which is at 4.5 m from the dish vertex. The measured return loss is much more complex than what is found from simulation. While the simulated return loss of the feed structure shows two resonant peaks around 120 and 160 MHz, the feed resonance occur at slightly higher frequencies. Notable are the
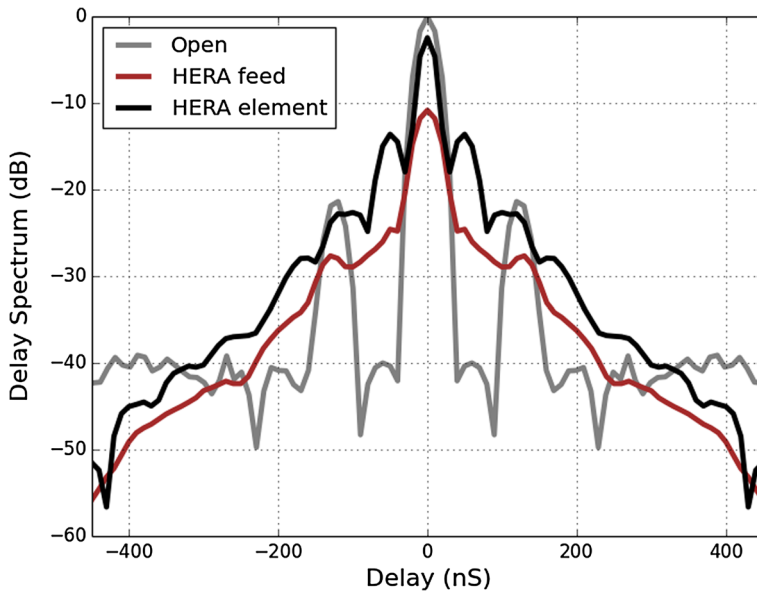
Fig. 5 Delay spectrum of the HERA feed (brown) estimated by taking the Fourier transform of the measured return loss of power at the feed output (upper panel in Fig. 4). The feed, when suspended on the dish results in a more complex return loss as shown in the lower panel of Fig. 4 and corresponding delay response is shown here in black. A balun with impedance transformation ratio 2 : 1 and input return loss of 22 dB across the band is used for converting the antenna balanced output to unbalanced output voltage. Balun response is embedded in the measurements. Delay spectrum of the open load (gray) shows the reflections at the VNA input
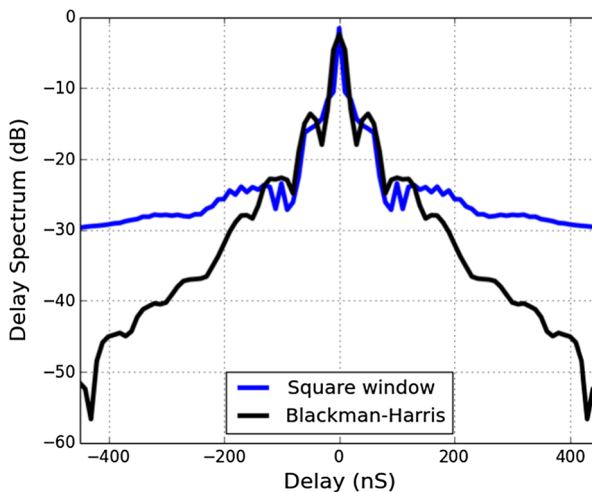

Fig. 6 Effect of finite bandwidth on estimation of delay spectrum: Blue line shows the delay spectrum of the HERA element computed from the measured data which is band limited between 100 to 200 MHz. Black line shows the delay spectrum estimated from the same data set after multiplying the data by a Blackman Harris window. The delay spectrum of the windowed data set shows significant reduction in the instrument response at higher delays

Table 1 System delay scale

Roundtrip Delay (ns)	Length scale (m)	Source
30	4.5	Dish apex
5.7	1.72	Feed Cavity
120	15	VNA Input

difference in the shape of the resonant peaks. While the simulated response shows very wide resonant peaks, as expected from these dipole structures, the measured return loss has a narrow peak at its low frequency resonance. The dominant term in the expression of return loss of the HERA element in receiving mode (10) is the zero delay term $(1 + \Gamma_f)$. Hence the feed return loss and especially the shape of the low frequency resonant peak dominates the overall shape of the delay spectrum in Fig. 7. The simulated return loss of the feed shows smooth variation across the band and wide resonant peaks resulting in a narrow delay spectrum.

4.3.2 CST Time domain simulation

We also compare our measurements with the time domain simulation presented in [12] in Fig. 7. In this simulation, the transient voltage response i.e the unit impulse response of the HERA element is determined as a function of time when it is subjected to a plane wavefront. The commercial numerical simulation software Microwave Studio, developed by Computer Simulation Technology is used for the
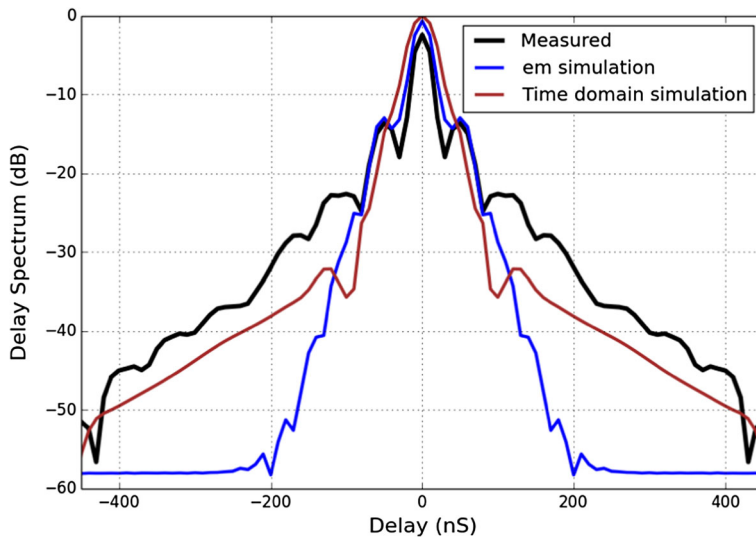

Fig. 7 Delay spectrum of HERA element estimated from the reflectometry measurements by a vector network analyzer compared to the delay spectrum estimated from the EM simulation using HFSS and time domain simulation using CST

simulation. The simulation assumed a constant 125 Ω impedance at the dipole terminal. Therefore, delay spectrum estimated from this simulation only has the effects of chromaticity introduced due to the structural reflections from the antenna and did not include the antenna mode scattering which is a function of frequency if the terminal impedance is frequency dependent. In practice, dipole impedance is function of frequency that results in variation of return loss with frequency. This results in deviation between the simulated delay response and the delay spectrum estimate of our measurements. The simulation and measurements both agree in one aspect. Our measurement also confirms that reflections from the feed structure dominate at lower delays and this is neither an attribute of the reflector dish response nor it is a computational artifact such as windowing.

4.3.3 Foreground simulation

We also compare our measurement with the foreground simulation of [42] as shown by the shaded regions in the first panel of Fig. 8. The shaded region of each panel shows the minimum EoR to foreground power ratio required for detection of the 21 cm power spectrum at those individual delays (or in $k_\parallel$ modes). This ratio is computed by using a achromatic antenna beam and the sky models. Diffused foreground sky model is incorporated from [8] whereas the point source contribution is estimated by combining the NRAO VLA Sky Survey (NVSS) at 1.42 GHz [6], Sydney University Molonglo sky Survey (SUMSS) [3, 20] at 843 MHz. The EoR signal is simulated by using 21cmFAST [22]. The model parameters used for the EoR signal simulation are : Virial temperature of minimum mass of dark matter halos that host ionizing sources, $T_{vir}^{min} = 2 \times 10^4$ K, Ionizing efficiency $\eta = 20\%$, mean free path of UV photons $R_{mfp} = 15$ Mpc. For these model parameter values, the redshift of 50% reionization is predicted to be at $z = 8.5$ at 150 MHz. The detailed description for the choice of the EoR model parameters can be found in [36].

The EoR and foreground power spectra are shown by the blue and the orange curve in Fig. 9. The details of the power spectrum computation are given in Section 5. The computed power spectra are associated with the shaded gray regions in following way. For simplicity, we inspect the effect of the foreground a particular delay, for example, say at $t = 200$ ns. The foreground power spectrum amplitude will need varied attenuation at different point on the the delay axis. For a given separation in delay, for example, at 200 ns, the foreground power spectrum amplitude should reduce from 10^15 (at delay t=0) to 10^4 mk^2. This requires a 110 dB attenuation of power spectrum amplitude or roughly 55 dB attenuation of power (visibility). For the same separation in delay, i.e 200 ns, the foreground power spectrum amplitude at 300 ns should be attenuated from 10^{14} to 10^4 mk^2 which is roughly 100 dB i.e 50 dB attenuation of the foreground power relative to the EoR. At $t = 400$ ns, the foreground should be attenuated from 10^{11} to 10^3 mk^2 between $t = 200$ to 400 ns which is roughly 80 dB attenuation of the foreground power spectrum amplitude or or 40 dB attenuation of the foreground power relative to the EoR. For the separation in delay $\tau = 200$ ns, any two points in delay space will need different attenuation of foreground power with respect to the EoR power and the maximum foreground power attenuation required will be 55 dB for the delays where foreground has the
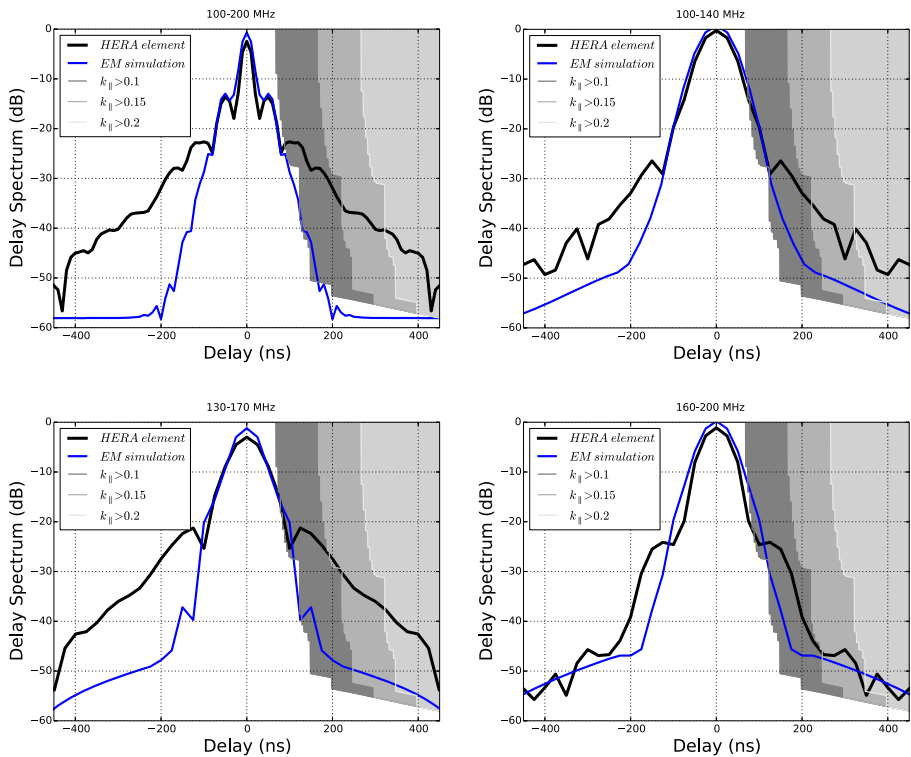
Fig. 8 Delay response of the instrument (black) estimated from measurements of the complex return loss of the HERA element. The blue curve shows the same estimated from the EM simulation of the HERA element corrected for the zero delay response. From right to left: the shaded gray regions show the minimum foreground attenuation relative to the EoR power required to detect the EoR power at a given delay (or in corresponding $k_\parallel$ mode). At a given delay, detection of EoR power spectrum at smaller $k_\parallel$ mode requires higher attenuation of the foreground power. This is shown by different shaded region each represening a minimum $k_\parallel$ mode that can be probed for that particular foreground attenuation profile in the delay domain. The instrument delay response estimated over the full band is dominated by the sharpest feature present in the observation band. At 120 MHz, the feed impedance is best matched to the 50 Ω reference impedance providing a very low value of return loss. This feature, when Fourier transformed to delay domain results in a wide response. At higher frequencies, the measured return loss varies smoothly with frequency resulting in narrow delay response of the instrument

highest magnitude. The maximum required attenuation of the foreground power at various values of τ is plotted in the gray shaded region for different values of τ.

The EoR to foreground power ratio shows that for a given delay mode, for a particular frequency, a successful power spectrum detection at a lower $k_\parallel$ mode requires a higher foreground power attenuation relative to the EoR power compared to a higher $k_\parallel$ mode. This simulation provides a baseline for the system performance evaluation with a conservative strategy of pure foreground avoidance without any foreground mitigation strategy. The measurement differs from the simulation in one aspect. Simulation includes the achromatic antenna gain excluding the return loss of of power at the antenna terminal due to frequency dependent antenna impedance. This effect is
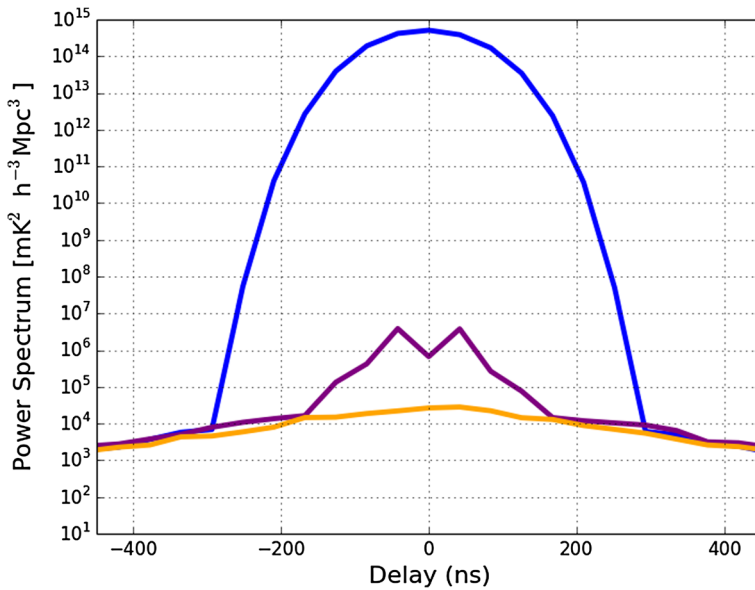
Fig. 9 Blue: Power spectrum of the sky signal estimated from the simulated visibility with two adjacent HERA elements and the foreground, EoR model described in Section 4.3.3. Orange: Power spectrum of only the EoR signal. Purple: Power spectrum estimate of the sky signal after weighting the simulated visibility by the inverse of the covariance matrix computed from the simulated data

included in the measurements. If included in the model, these limits would provide more conservative estimates of the required instrument response which will be even harder to achieve.

4.3.4 Delay spectrum of subbands

In the HERA analysis, the 21 cm power spectrum is estimated by discretizing the observed data along the line of sight distance i.e in frequency or redshift and in the plane of the sky k [17]. At particular redshift, the bandwidth of observation is so chosen that over the corresponding Δz, the 21 cm signal does not significantly evolve. Typically, the 21 cm brightness temperature fluctuation evolves over redshift scale $\Delta z > 0.5$ [15, 18]. Therefore, the delay spectrum is estimated over smaller bandwidths.

We estimate the instrument delay spectrum over various sub bands between 100 to 200 MHz as shown in Fig. 8. Each panel of Fig. 8 shows the delay spectrum estimated from the return loss measurement of the HERA element between 100–200, 100–140, 130–170, 160 to 200 MHz respectively. Each panel also compares the delay spectrum estimate obtained EM simulation of [9] at various subband. Subband delay spectra are wider compared to full band delay spectrum. The shape of the resonant peaks determines the roll off rate of the delay spectrum at all frequency ranges. At higher

frequency, our measurement closely follows the EM simulations except around 80-120 ns where the cable reflection between the antenna and the backend manifests itself.

The shaded regions represent the EoR to Foreground power ratio simulated across the entire band. The HFSS simulation of chromatic antenna beam varies smoothly across frequency resulting in no significant changes in this simulation at various sub bands. HERA system performance conforms directly to the limits as posed by simulations, at frequencies >160 MHz. With the measured system response including the multiple reflections, the instrument would be able to probe the spatial modes of interest $k_{\parallel} > 0.2h$ Mpc^{-1} with very little foreground bleeding around $k_{\parallel} \approx 0.2h$ Mpc^{-1}. At other frequencies, it is possible to do a successful measurement by weighting down the foreground contribution in the measured data. This is discussed in the following section.

The HERA analysis pipeline for power spectrum estimation exploits the inverse covariance weighting to reduce the foreground contribution to the measured visibility data. In the light of this analysis technique we further investigate the limits of EoR to foreground power ratio from what is established by conservative estimates of [42]. In the following section we briefly describe the power spectrum estimation technique used in HERA analysis and inverse covariance weighting. We evaluate the instrument delay response in the context of covariance weighting.

5 Revised delay spectrum specification using inverse covariance weighting

Results presented in previous sections focused on the delay-domain performance of the prototype HERA element which convolves with the delay spectrum of the sky signal and produce the delay spectrum. In the delay domain, after convolution with the instrument response, the foreground response must fall below the amplitude of the 21 cm EoR signal to avoid a systematic bias. This simple analysis omits the suppression of foreground systematics that are a feature of more sophisticated power spectrum estimation techniques. In this section, we re-evaluate the specification for the delay-domain performance of the HERA element in light of the HERA power spectrum estimation method using the optimal quadratic estimator (OQE). The OQE formalism has been outlined in extensive detail in [1, 10, 16, 17, 45]. In order to determine the effect of covariance in the measured data, we notationally describe the OQE formalism here. The 21 cm power spectrum $P_{21}(k_{\perp}, k_{\parallel})$ integrated over a range of $k_{\parallel}, k_{\perp}$, is estimated as the band power $\hat{p}_{\alpha}$, where α represents a range of $k_{\parallel}, k_{\perp}$. The major steps of the OQE formalism are,

The unnormalized band power $\hat{q}_{\alpha}$, estimated from the data vector $\mathbf{x}$ of measured visibilities is

$$\hat{q}_{\alpha} = \mathbf{x}^T E^{\alpha} \mathbf{x}, \tag{13}$$

E^{α} is a symmetric matrix operation denoting the Fourier transform of the data, binning, and foreground reduction. The normalized estimate of the power spectrum

is,

$$\hat{p}_\alpha = M\hat{q}_\alpha \tag{14}$$

where M is the normalization matrix. The true power spectrum p_α is

$$\hat{p}_\alpha = Wp_\alpha \tag{15}$$

where W is the window function matrix,

Various binning and foreground reduction techniques result in different forms of E^α resulting in estimates of $\hat{p}_\alpha$ with different statistics. A possible choice of E^α is

$$E^\alpha = \frac{1}{2}C^{-1}Q_\alpha C^{-1} \tag{16}$$

where $C = \langle \mathbf{xx}^t \rangle$ is the covariance matrix of the data vector $\mathbf{x}$. Q_α is a matrix operator that Fourier transforms the visibilities along the frequency axis and maps them into the $\mathbf{k}$ space. The critical step in the OQE formalism for power spectrum estimation is the weighting of the data by the inverse of its covariance. This can result in orders-of-magnitude reduction in the foreground power relative to the EoR signal. To derive a delay-spectrum specification for a prototype HERA element using the inverse covariance weighting, we begin with the simulations of [42] and use OQE formalism to estimate the amplitude of the power spectrum from a simulated data vector $\mathbf{x}$ which contains contributions from the EoR, the foreground and the instrument noise. The covariance matrix is estimated from 80 different realizations of the data vector $\mathbf{x}$ between $0-24$ h of LST. The power spectrum, estimated using one realization of $\mathbf{x}$, with and without covariance weighting are shown in Fig. 9. The orange curve represents the power spectrum computed from the EoR model for two adjacent HERA elements with a given baseline orientation. The blue curve shows the power spectrum of the observed sky signal including both foreground and the EoR using the delay transform technique after appropriate windowing. Here, the contribution from the bright foregrounds dominate the lower delay modes, making separation of the EoR from the foreground impossible up to delays ≈ 300 ns. The power spectrum estimated after weighting the data by the inverse of the covariance matrix is illustrated by the purple curve in the plot. Weighting the simulated data by the covariance matrix which is also estimated from the simulated visibility dramatically reduces the foreground power relative to the EoR signal at low delays, opening up the possibility of estimating the EoR power spectrum at those delays.

In a simple delay-transform power spectrum estimation, the chromatic antenna response is convolved with the foreground signal in delay domain. As described in [42], this enables us to set a specification for the reflectometry of the HERA element as a function of delay, as illustrated by the gray shaded regions in Fig. 10. This relationship is not so straightforward when using optimal quadratic power-spectrum estimation. For example, a direction-independent bandpass shape that multiplies the foreground signal falls into a single delay mode that can be downweighted essentially to zero. This makes it problematic to interpret the output power spectrum in the light of reflectometry constraints which comes from the beam integrated reflectometry measurements. Without knowing in detail the direction dependence of the HERA element chromaticity, it is impossible to estimate exactly how many Eigen modes will be occupied by the systematics arising from the foreground-HERA element interaction.
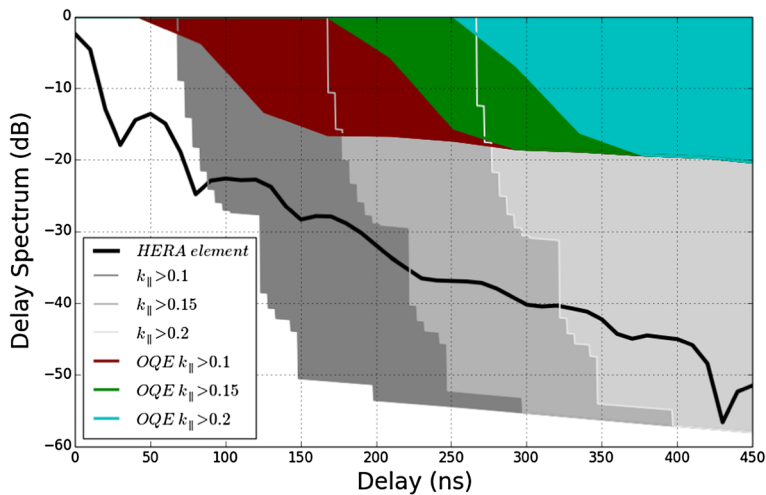
Fig. 10 Delay spectrum of HERA element estimated from the reflectometry measurements by a vector network analyzer (black). The colored region shows the revised EoR to foreground power ratio as a function of the separation in delay space after weighting the simulated visibility by the inverse of its covariance. Due to inverse covariance weighting of the visibility, the foreground contribution at each delay is reduced relaxing the limits on the required foreground attenuation relative to the EoR by about 30 dB at each delay. In comparison to this revised specification derived from the sky power simulation, the HERA element delay response demonstrates its capacity for a successful power spectrum detection without any additional design improvement

In a relatively conservative estimate, we simply use the inverse covariance weighted foreground power spectrum from simulations as an effective input foreground amplitude and repeat the translation to a reflectometry specification as before. The result is illustrated by the colored shaded regions in Fig. 10. This approach ignores the ability of OQE to identify and invert instrumental covariances, making it a relatively conservative standard. On the other hand, should the number of direction-dependent spectral eigenmodes of the dish become large, this approach could potentially underestimate the impact of dish chromaticity. Therefore, we present it as a demonstration that our reflectometry specifications could be substantially less stringent for HERA's OQE pipeline, but suggest not over-interpreting the exact level of the implied specification without a detailed analysis of the direction dependence of the reflectometry results.

6 Conclusion

The interplay between the extremely bright sky signal and the system response has remained somewhat undetermined for the first generation 21 cm experiments such as MWA, LOFAR, PAPER. With the theory of redshifted 21 cm experiments very well evolved, it is now absolutely necessary to quantify the instrumental limits of these measurements in order to produce accurate power spectrum estimates. The delay-domain performance of the HERA dish is central to HERA's function as a power

spectrum instrument. In this paper, we studied the performance of a prototype HERA element in both frequency as well as delay domain. We introduced a mathematical formalism that explicitly relate the delay response of the HERA element to EoR to foreground power ratio in the delay domain. The effects of multiple reflections in a HERA element is investigated in detail and their effects on the measured visibility is estimated. Reflectometry measurements characterized HERA's performance in delay domain domain and, as (9) shows, these measurements must be adjusted for a difference in transmission/reception at the first feed encounter in order to be interpreted as the delay response of a HERA element relative to an incident plane wave from the sky. It is also shown that the windowing the measured data by the Blackman-Harris window, shown in [42] is critical for accurately measuring the antenna delay response at higher delays, where sidelobes from much higher amplitude responses at small delays can easily dominate. Windowing the measured data conclusively shows that the lower delay response results from the structural reflections in the feed. Given the critical nature of the windowing function, it is recommended that all reflectometry measurements be performed in the frequency domain, so that the data could be Fourier transformed with the appropriate window. The delay spectrum estimates are compared with the electromagnetic simulation of the HERA element [9, 12]. The same is then compared with the estimates derived from the foreground simulation of [42]. The performance is also evaluated in the light of HERA power spectrum estimation technique using inverse covariance weighting formalism. The reflectometry measurements demonstrate the performance of the HERA element including it intrinsic chromaticity and chromaticity generated due to multiple reflections in the system. The prototype HERA element delay response, in conjunction with the inverse covariance method of foreground suppression, indicates that the HERA prototype element satisfies the necessary condition to make a successful power spectrum measurement for the spatial modes as low as $k_{\parallel} > 0.1h$ Mpc^{-1}. Taken all together, we conclude that the HERA antenna element, with a PAPER-style crossed dipole feed and cylindrical cage, satisfies the criteria necessary to meet its science observation goal between 100–200 MHz.

References

1. Ali, Z.S., Parsons, A.R., Zheng, H., et al.: PAPER-64 constraints on reionization: the 21 cm power spectrum at z = 8.4. ApJ **809**, 61 (2015)
2. Barry, N., Hazelton, B., Sullivan, I., Morales, M.F., Pober, J.C.: Calibration requirements for detecting the 21 cm epoch of reionization power spectrum and implications for the SKA. MNRAS **461**, 3135 (2016)

3. Bock, D.C.-J., Large, M.I., Sadler, E.M.: Instrumentation: interferometers, radio continuum, surveys. AJ **117**, 1578 (1999)
4. Bowman, J.D., Morales, M.F., Hewitt, J.N.: Foreground contamination in interferometric measurements of the redshifted 21 cm power spectrum. ApJ **695**, 183 (2009)
5. Bowman, J.D., Rogers, A.E.E.: A lower limit of $\Delta z > 0.06$ for the duration of the reionization epoch. Nature **468**, 796 (2010)
6. Condon, J.J., Cotton, W.D., Greisen, E.W., et al.: The NRAO VLA sky survey. AJ **115**, 1693 (1998)
7. Datta, A., Bowman, J.D., Carilli, C.L.: Bright source subtraction requirements for redshifted 21 cm measurements. ApJ **724**, 526 (2010)
8. de Oliveira-Costa, A., Tegmark, M., Gaensler, B.M., et al.: A model of diffuse Galactic radio emission from 10 MHz to 100 GHz. MNRAS **388**, 247 (2008)
9. DeBoer, D.R., Parsons, A.R., Aguirre, J.E., et al.: Hydrogen Epoch of Reionization Array (HERA). Publ. Astron. Soc. Pac. **129**(2017), 045001 (2016)
10. Dillon, J.S., Liu, A., Tegmark, M.: A fast method for power spectrum and foreground analysis for 21 cm cosmology. Phys. Rev. D **87**, 043005 (2013)
11. Dillon, J.S., Liu, A., Williams, C.L., et al.: Overcoming real-world obstacles in 21 cm power spectrum estimation: A method demonstration and results from early Murchison Widefield array data. Phys. Rev. D **89**, 023002 (2014)
12. Ewall-Wice, A., Bradley, R., Deboer, D., et al.: The HERA Dish II: electromagnetic simulations and science implications. Astrophys. J. **831**(2), 17 (2016). article id. 196
13. Furlanetto, S.R., Oh, S.P., Briggs, F.H.: Cosmology at low frequencies: The 21 cm transition and the high-redshift Universe. Phys. Rep. **433**, 181 (2006)
14. Kohn, S.A., Aguirre, J.E., Nunhokee, C.D., et al.: Constraining polarized foregrounds for EoR experiments I: 2D power spectra from the PAPER-32 imaging array. ApJ **823**, 88 (2016)
15. Lidz, A., Zahn, O., McQuinn, M., Zaldarriaga, M., Hernquist, L.: Detecting the rise and fall of 21 cm fluctuations with the Murchison widefield array. ApJ **680**, 962 (2008)
16. Liu, A., Parsons, A.R., Trott, C.M.: Epoch of reionization window. II. statistical methods for foreground wedge reduction. Phys. Rev. D **90**, 023018 (2014)
17. Liu, A., Parsons, A.R., Trott, C.M.: Epoch of reionization window. I. Mathematical formalism. Phys. Rev. D **90**, 023019 (2014)
18. Loeb, A., Zaldarriaga, M.: Measuring the small-scale power spectrum of cosmic density fluctuations through 21cm tomography prior to the epoch of structure formation. Phys. Rev. Lett. **92**, 211301 (2004)
19. Madau, P., Meiksin, A., Rees, M.J.: 21 Centimeter tomography of the intergalactic medium at high redshift. ApJ **475**, 429 (1997)
20. Mauch, T., Murphy, T., Buttery, H.J., et al.: SUMSS: A wide-field radio imaging survey of the southern sky - II. The source catalogue. MNRAS **342**, 1117 (2003)
21. Mellema, G., Koopmans, L.V.E., Abdalla, F.A., et al.: Reionization and the cosmic dawn with the square kilometre array. Exp. Astron. **36**, 235 (2013)
22. Mesinger, A., Furlanetto, S., Cen, R.: 21CMFAST: a fast, seminumerical simulation of the high-redshift 21-cm signal. MNRAS **411**, 955 (2011)
23. Morales, M.F., Hazelton, B., Sullivan, I., Beardsley, A.: Four fundamental foreground power spectrum shapes for 21 cm cosmology observations. ApJ **752**, 137 (2012)
24. Morales, M.F., Wyithe, J.S.B.: Reionization and cosmology with 21-cm fluctuations. ARA&A **48**, 127 (2010)
25. Neben, A.R., Bradley, R.F., Hewitt, J.N., et al.: The hydrogen epoch of reionization array dish. I. Beam pattern measurements and science implications. ApJ **826**, 199 (2016)
26. Paciga, G., Chang, T.-C., Gupta, Y., et al.: The GMRT Epoch of reionization experiment: a new upper limit on the neutral hydrogen power spectrum at z8.6. MNRAS **413**, 1174 (2011)
27. Parsons, A.R., Backer, D.C.: Calibration of low-frequency, wide-field radio interferometers using delay/delay-rate filtering. AJ **138**, 219 (2009)
28. Parsons, A.R., Backer, D.C., Foster, G.S., et al.: The precision array for probing the Epoch of reionization: eight station results. AJ **139**, 1468 (2010)
29. Parsons, A., Pober, J., McQuinn, M., Jacobs, D., Aguirre, J.: A sensitivity array-configuration study for measuring the power spectrum of 21 cm emission from reionization. ApJ **753**, 81 (2012)
30. Parsons, A.R., Pober, J.C., Aguirre, J.E., et al.: A Per-baseline, delay-spectrum technique for accessing the 21 cm cosmic reionization signature. ApJ **756**, 165 (2012)

31. Parsons, A.R., Liu, A., Aguirre, J.E., et al.: New limits on 21 cm Epoch of reionization from PAPER-32 consistent with an x-ray heated intergalactic medium at z = 7.7. ApJ **788**, 106 (2014)
32. Patra, N., Subrahmanyan, R., Raghunathan, A., UdayaShankar, N.: Bandpass calibration of a wideband spectrometer using coherent pulse injection. Exp. Astron. **36**, 319 (2013)
33. Patra, N., Subrahmanyan, R., Sethi, S., Udaya Shankar, N., Raghunathan, A.: Saras measurement of the radio background at long wavelengths. ApJ **801**, 138 (2015)
34. Patra, N., Bray, J.D., Roberts, P., Ekers, R.D.: Bandpass calibration of a wideband spectrometer using coherent pulse injection. Exp. Astron. **43**(2), 119–129 (2017)
35. Pober, J.C., Parsons, A.R., Aguirre, J.E., et al.: Opening the 21 cm Epoch of reionization window: measurements of foreground isolation with PAPER. ApJ **768**, L36 (2013)
36. Pober, J.C., Liu, A., Dillon, J.S., Aguirre, J.E., et al.: What next-generation 21 cm power spectrum measurements can teach us about the Epoch of reionization. ApJ **782**(2), article id. 66 25 (2014)
37. Presley, M., Liu, A., Parsons, A.: Measuring the cosmological 21 cm monopole with an interferometer. arXiv:1501.01633 (2015)
38. Pritchard, J.R., Loeb, A.: Evolution of the 21cm signal throughout cosmic history. Rep. Prog. Phys. **75**, 086901 (2012)
39. Shaver, P.A., Windhorst, R.A., Madau, P., de Bruyn, A.G.: Can the reionization epoch be detected as a global signature in the cosmic background? A&A **345**, 380 (1999)
40. Sokolowski, M., Tremblay, S.E., Wayth, R.B., Tingay, S.J., et al.: BIGHORNS - Broadband Instrument for Global HydrOgen ReioNisation Signal. Publ. Astron. Soc. Aust. **32**, id.e004 18 (2015)
41. Thyagarajan, N., Udaya Shankar, N., Subrahmanyan, R., et al.: A study of fundamental limitations to statistical detection of redshifted H I from the Epoch of Reionization. ApJ **776**, 6 (2013)
42. Thyagarajan, N., Parsons, A.R., DeBoer, D.R., et al.: Effects of antenna beam chromaticity on red-shifted 21 cm power spectrum and implications for hydrogen Epoch of Reionization array. ApJ **825**, 9 (2016)
43. Thyagarajan, N., Jacobs, D.C., Bowman, J.D., et al.: Foregrounds in wide-field redshifted 21 cm power spectra. ApJ **804**, 14 (2015)
44. Tingay, S.J., Goeke, R., Bowman, J.D., Emrich, D., Ord, S.M., Mitchell, D.A., Morales, M.F., et al.: The Murchison widefield array: the square kilometre array precursor at low radio frequencies. Publ. Astron. Soc. Aust. **30**, id.e007 21 (2013)
45. Trott, C.M., Wayth, R.B., Tingay, S.: The impact of point-source subtraction residuals on 21 cm Epoch of Reionization estimation. ApJ **757**, 101 (2012)
46. van Haarlem, M.P., Wise, M.W., Gunst, A.W., et al.: LOFAR: the low-frequency array. A&A **556**, A2 (2013)
47. Vedantham, H., Udaya Shankar, N., Subrahmanyan, R.: Imaging the Epoch of reionization: limitations from foreground confusion and imaging algorithms. Mon. Not. R. Astron. Soc. **450**(3), 2291–2305
48. Voytek, T.C.: PhD thesis, Carnegie Mellon University; Probing the Dark Ages at z20: The SCI-HI 21 cm All-sky Spectrum Experiment (2015)